




## A Comparative Analysis of UAV-RTK and UAV-PPK Methods in Mapping Different Surface Types

Remzi Eker<sup>1\*</sup> , Ece Alkan<sup>2</sup> , Abdurrahim Aydın<sup>2</sup> 

<sup>1</sup> İzmir Katip Çelebi University, Faculty of Forestry, 35620, İzmir, Turkey

<sup>2</sup> Düzce University, Faculty of Forestry, 81620 Düzce, Turkey

### Abstract

This study aimed to compare unmanned aerial vehicle (UAV) based real-time kinematic (RTK) and post-processing kinematic (PPK) methods via five approaches: an RTK-CORS method (M1), a short-baseline PPK method obtaining corrections from a GNSS base station (M2), and three long-baseline PPK methods that obtained corrections from the three Turkish RTK-CORS network TUSAGA-Aktif reference stations (M3: IZMI, M4: CESM, and M5: KIKA). The comparison was based on the accuracy of the corrected camera positions, the average error of the camera locations computed in the photo-alignment and optimization process, georeferencing errors of the models via nine GCPs based on four scenarios, and Root Mean Square (RMS) errors in the Z-direction for different surface types (i.e. roads, shadows, shrubs, boulders, trees, and ground). For the surface types of “ground”, “roads”, and “shrubs”, RMS error rates were obtained 10 cm lower than that of other surface types in all methods except M4. The greatest differences were obtained over trees and shadowed areas. The conclusion of these comparisons was that the lowest RMS error rate was determined on a solid textured surface. The consideration of mean RMS error regardless of surface type in such model comparisons is misleading.

**Keywords:** Accuracy comparison, GNSS, Photogrammetry, RTK/PPK, Surface Types, UAV

### 1. Introduction

In last decades, unmanned aerial vehicle (UAV) systems have been extensively applied in scientific and practical areas as an alternative remote sensing platform (Nebiker et al., 2008; Wallace et al., 2012) and/or a new photogrammetric measurement tool (Eisenbeiss, 2009). Today, UAVs can be seen in a large variety of different disciplines and specific applications including agriculture (Honkavaara et al., 2013; Tokekar et al., 2016; Radoglou-Grammatikis et al., 2020), forestry (Lisein et al., 2013; Yuan et al., 2015; Wallace et al., 2016; Thiel and Schmulius, 2017; Akgul et al., 2018; Gülci, 2019; Jurjevic et al., 2020), natural hazard monitoring and management (Giordan et al., 2017; Gomez and Purdie, 2016), landslide evaluation (Niethammer et al., 2009; Carvajal et al., 2011; Lucieer et al., 2014; Turner et al., 2015; Lindner et al., 2016; Mateos et al., 2017; Eker et al., 2018; 2021), snow and avalanche studies (Vander Jagt et al., 2015; Bühler et al., 2016; De Michele et al., 2016; Adams et al., 2018; Eker et al., 2019), flood monitoring and mapping (Abdelkader et al., 2013; Langhammer et al., 2017; Annis et al., 2020), rockfall modeling and mapping (Saroglu et al., 2018), and archaeology (Fernández-Hernandez et al., 2015; Campana, 2017). The frequent use of this technology is mostly due to the advantages of UAV systems (Torresan et al., 2017) such as: (1) low material and operational costs and high-intensive data collection,

(2) flexibility in hosting different kinds of sensors that can be selected depending on the parameter under investigation, (3) control over timing of flights enabling the user to optimize the exact time, and (4) data acquisition with very high spatial resolution. Along with their benefits given above, low-altitude small-UAV systems have some limitations such as flight endurance and data acquisition over large areas. They have limited payload capacities and require the development of massive data processing capabilities in photogrammetric modeling depending on the size of the surveying area (Matese et al., 2015).

Remote sensing requires a UAV system that consists of an aircraft component, sensor payload, and ground control station (Watts et al., 2012). The aircraft component, which can be divided into different categories depending on the technical structure and flying properties (Watts et al., 2012), is equipped with global navigation satellite system (GNSS) receivers, inertial measuring units (IMU), and other sensors, allowing autonomous navigation via autopilot along flight paths to guarantee sufficient image coverage and overlap, and enabling the user to estimate the expected product accuracy prior to the flight (Eisenbeiss, 2009; Remondino et al., 2011; Colomina and Molina, 2014). These low-altitude small-UAV systems generally carry lightweight sensor payloads such as consumer digital cameras, or combinations of imaging systems. These

\*Corresponding Author: Tel: +90 232 3293535/5227 E-mail: [remzi.eker@ikc.edu.tr](mailto:remzi.eker@ikc.edu.tr)

Received 16 May 2021; Accepted 17 June 2021

This work is licensed under a Creative Commons Attribution-NonCommercial 4.0 International License



imaging systems can include the visible spectrum, infrared and the thermal spectrum (i.e., multi- or hyperspectral sampling), miniature radar, passive microwave radiometers, and light-detection and ranging (LIDAR) sensors (Colomina and Molina, 2014; Sugiura et al., 2007; Evaerts, 2015).

Photogrammetry using UAVs is based on high-resolution overlapped images used to create digital elevation models (DEMs) and orthophotos by applying structure-from-motion (SfM) techniques and Multiview Stereopsis (MVS). The SfM is a photogrammetric method for creating 3D (three-dimensional) models of a feature or topography from overlapping 2D photos taken from many locations and orientations in order to reconstruct the photographed scene (Shervais, 2015). The SfM process starts by acquiring photographs with sufficient overlap (e.g., 80-90%) from multiple positions and/or angles (Lucieer et al., 2014). The MVS is a technique that is used for densification of the resulting point cloud from SfM. In fact, SfM does not require information on the position of cameras or multiple control points prior to image acquisition because the position, orientation, and geometry are reconstructed using automatic matching of features in multiple images (Westoby et al., 2012). However, the resulting model has no proper scale unless spatial reference information is used. The absolute orientation needed for the solution of such scaling problems of the model can be achieved in two ways: using ground control points (GCPs) or GNSS-tagged imagery (Tomaščík et al., 2019).

Georeferencing of UAV-based models is mostly carried out using GCPs surveyed with terrestrially based methods (GPS/GNSS or tachymetry). The use of GCPs for georeferencing of models provides reliable positioning; however, the number and spatial distribution of the GCPs have an important effect on model accuracy (Sanz-Ablanedo et al., 2018; Zhang et al., 2019). In addition, the use of GCPs allows improved camera self-calibration, and reduces the magnitude of dome errors (James and Robson, 2014; Harwin et al., 2015; James et al., 2017). Agüera-Vega et al. (2017) assessed UAV-based model accuracy using a varying number of GCPs (4 – 20), and they concluded that both horizontal and vertical accuracy increased in parallel with the number of GCPs used. Moreover, Eker et al. (2019) generated 190 artificial GCPs from the first 3D model belonging to a time series of UAV flights in order to increase model accuracy (i.e., avoiding bending or doming effects) and to obtain well-registered models. Even though an increased number of GCPs and their regular spatial distribution have a positive effect, surveying them is labor-intensive and sometimes risky amid steep slopes (Zhang et al., 2019). When the study area is situated in mountainous areas with dangerous, hard-to-access steep slopes, GCP surveys can sometimes be risky because of potential hazards such as landslides, rockfalls, etc. In addition, dense forests do not facilitate the surveying of regularly distributed GCPs over the flight area because

the tree canopies cover the GCPs in the successive images, even though the GCPs are marked in small gaps within the forest.

As previously studies indicated, tagging images with position information from GNSS receivers (i.e., direct georeferencing based on GNSS) integrated into UAV systems is an alternative method for surveying GCPs. The utilization of the direct georeferencing approach has the potential of avoiding or mitigating the need for GCPs. Most of the common UAV platforms preferred in mapping applications have a GNSS receiver that can be used to add positional information to the exchangeable image file (EXIF) metadata of the images acquired during flight (Tomaščík et al., 2019). However, the accuracy of the typical single-frequency GNSS receivers on the UAV platforms is in the range of meters. Consequently, when high-accuracy models are demanded, the positional information obtained from such GNSS receivers is insufficient. At present, differential GNSS solutions (e.g., multi-frequency and multi-constellation GNSS receivers) have been used that enable the accurate measurement of the UAV-camera position and orientation by allowing measurement of the position parameters at the centimeter level (Rehak et al., 2013). This high-precision direct georeferencing involves the same strategies as those for traditional geodetic GNSS receivers, i.e., real-time kinematic (RTK) and post-processing kinematic (PPK) technologies (Taddia et al., 2020). For the application of differential GNSS solutions, two receivers are required: a base station and a rover moving between points of interest (Hofmann-Wellenhof et al., 2007). The base station broadcasts its well-known location together with the code and carrier measurements, and thus, the rover is able to fix the phase ambiguities and determine its location relative to the base with high precision. In RTK mode, the position information of the camera is determined with accuracy in the range of centimeters in real time as the drone flies. In PPK mode, as an alternative to RTK, all calculations required for position correction are made post flight. The GNSS observations are stored in a log file in Receiver Independent Exchange (RINEX) format (Taddia et al., 2020).

For differential GNSS solutions, however, it is not necessary to have a second receiver as a local base all the time. Alternatively, local services sharing base corrections over the Internet via NTRIP (Networked Transport of RTCM via Internet Protocol) technology can be a good option. In Turkey, an RTK-CORS network of continuously operating reference stations known as the “TUSAGA-Aktif” project (completed between 2006 and 2009) was established by Istanbul Kultur University in association with the General Directorate of Land Registration and Cadastre of Turkey, and the General Command of Mapping of Turkey. It also became under the sponsorship of the Turkish Scientific and Technical Research Agency (TUBITAK) (Mekik et al., 2011). The Turkish RTK-CORS network was established with a

total of 146 reference stations having baselines ranging from 70 to 100 km that, along with the control centers, provide RTK GPS positioning for 24 h/day extending over Turkey and Northern Cyprus (Yıldırım et al., 2011). Positioning corrections are calculated by the reference stations and sent to users from control centers via the Internet. In addition, for PPK positioning, RINEX data is collected by the reference stations at 1-s or 30-s time intervals, along with precise ephemeris data collected automatically by the system (Mekik et al., 2011).

The present study evaluated the accuracy of UAV RTK/PPK methods in the mapping of different surface types including roads, shadows, shrubs, boulders, trees, and ground. For this purpose, UAV data was acquired from two flights (one in RTK mode and the other in PPK mode) conducted using the same flight plan. In the RTK mode, base corrections were acquired via NTRIP technology. In the PPK mode, base corrections were acquired as RINEX data collected using both a local base

reference station and the three TUSAGA-Aktif reference stations closest to the study area (IZMI, CESH, and KIKA). In addition, the georeferencing error rates of models were compared based on different scenarios in order to evaluate the accuracy of the RTK/PPK methods without GCPs, and to determine whether using some GCPs is still a requirement for improving accuracy.

## 2. Material and Methods

### 2.1 Study area

The study was carried out over a forest area located in Bornova Forest Enterprise (İzmir Regional Directorate of Forestry in western Turkey) (Figure 1) covering 31 ha land. In WGS 1984 World Mercator coordinate system, the left and upper coordinates in decimal degrees of the area are 27.116 Lon and 38.554 Lat, and the right and lower coordinates are 27.124 Lon and 38.547 Lat, respectively. The mean altitude of the study area is 553 m AMSL (above mean sea level).

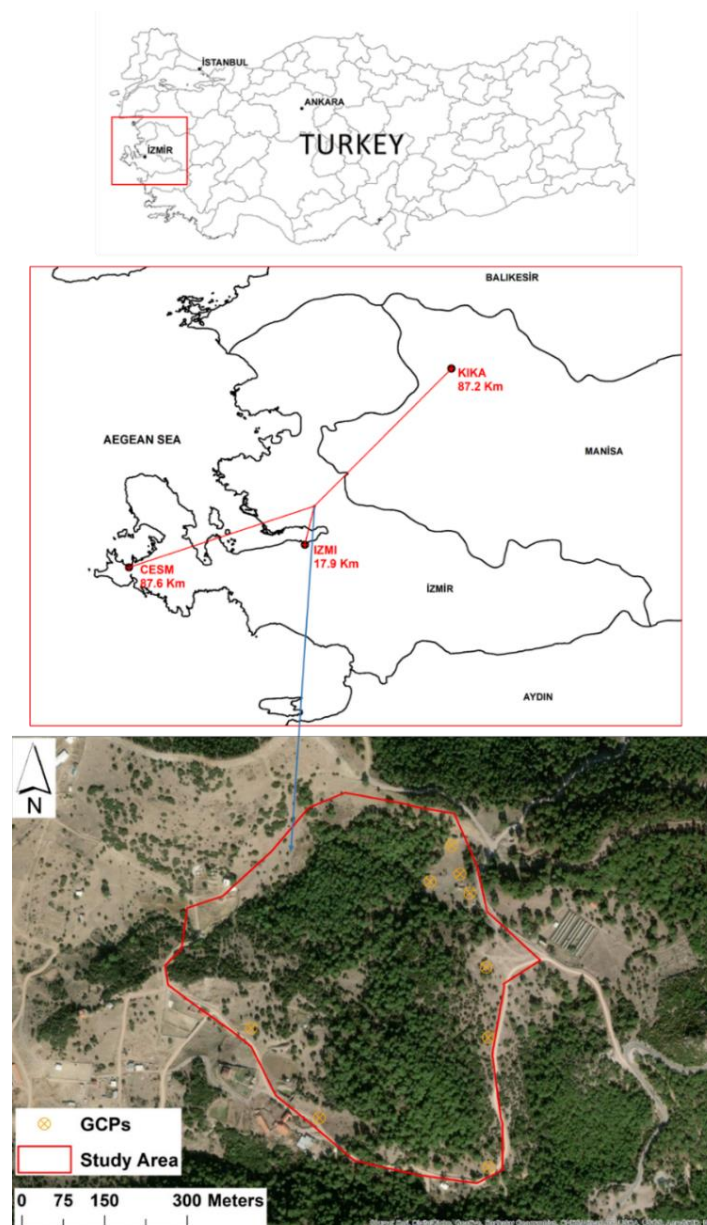


Figure 1. Study area: Location (Top), “TUSAGA-Aktif” reference stations (CESM, IZMI, and KIKA) and their proximity to the study area (Middle), and Surveyed GCPs (Bottom)

## 2.2. UAV flights and data acquisition

The DJI Phantom 4 RTK, a small four-propeller drone with an RTK module, was used for UAV data acquisition in the study (Figure 2). The aircraft is equipped with a 20-megapixel camera with a 1-inch CMOS sensor. The lens has a viewing angle of  $84^\circ$  with  $f/2.8 - f/1.1$  focal length and a focus range of  $1\text{ m} - \infty$ . Because of the high-resolution sensor, the UAV system can achieve a ground sample distance (GSD) of 2.74 cm at 100-m flight altitude. The system applies a rigorous calibration process to every single camera lens, with parameters saved in the metadata of each image. Thus, it allows each user to adjust the post-processing software individually. The aircraft is equipped with a GNSS module that enables reception of GPS (L1/L2), GLONASS (L1/L2), and Galileo (E1/E5a) satellites. This UAV system is capable of directing georeferencing of the images in real time with centimeter-level positioning accuracy. In addition, the UAV system stores satellite observation data to be used for PPK. For RTK mode, the DJI Phantom 4 RTK can be used together with the D-RTK 2 High Precision GNSS Mobile Station for direct georeferencing, or it can connect to the Internet to receive corrections using NTRIP technology via a 4G dongle or WiFi hotspot.

The present study aimed to evaluate the accuracy of the UAV-RTK and PPK methods in the mapping of different surface types. To this purpose, two UAV flights were carried out on 20 August 2020: one flight in RTK mode, and the other in PPK mode. The UAV system provides users with a DJI GS RTK app and a remote controller with a built-in screen, which presents an ultra-bright, 5.5-inch HD display. Users also have a streamlined control scheme for surveying missions and other data acquisition scenarios. In addition, they can also import KML/KMZ files to optimize the workflow for their missions. In this study, the flight plan was carried out in photogrammetry (3D) mode, allowing topography-adaptive flights. The SRTM 30-m digital elevation data was downloaded and then imported in “geotiff” format. The size of the flight area was small for a one-battery flight (31 ha); therefore, the mission image acquisition was planned from 120 m above ground level (a.g.l). Both forward and side image overlapping rates were set at 90%. Before the UAV flights were carried out, nine GCPs were surveyed at centimeter accuracy using the CHCN X91 GNSS receiver to ensure that the images to be acquired would be clearly visible (Figure 1). They were distributed randomly over area. For image acquisition in RTK mode, a 4G USB dongle was used to receive position corrections from the TUSAGA-Aktif reference stations using NTRIP technology via the Internet connection. Because a D-RTK 2 High-Precision GNSS Mobile Station was not available, this method will be referred to hereafter as RTK-CORS.

For image acquisition in PPK mode, first the “RTK function” was turned off. The UAV flight was then carried out with the same flight plan. When the UAV was

in the air, the rover observation file ending with “Rinex.obs” was saved directly onto the SD memory card. In addition, a base station file (RINEX observation data) was needed. Therefore, the CHCN X91 GNSS receiver was used as the solution for the short-baseline PPK positioning. The GNSS receiver was fixed with a tripod at a location with known coordinates where the GNSS satellite signals were not blocked by any large obstacles such as mountains or trees, and surveying was initiated in static mode at an antenna height of 193 cm. Since the RINEX observation data needed to cover the full period of the flight, the static survey was carried out for a time period lasting more than one hour, covering at least 15 min both before and after the UAV flight. The static survey was saved in the internal memory of the receiver as a log file with an extension of “.HCN”, which is a specific file format of used GNSS receiver, which was converted to RINEX observation data. CHCData software was used to accomplish the conversion of the base log file to RINEX (version 3.02). In addition, for the long-baseline PPK positioning solution, RINEX data (1-second interval) for the same date of the flight were obtained from the three TUSAGA-Aktif reference stations closest to the study area. These reference stations are officially listed as IZMI, CESM, and KIKA in the TUSAGA-Aktif network, and their proximity to the study area is 17.7 km, 70.7 km, and 78.1 km, respectively. The coordinates of these reference stations were obtained from the official TUSAGA-Aktif website. The correction of camera positions for the images acquired in PPK mode was made using CHC Geomatics Office 2 software (Figure 3). The rover and base observation files, i.e., the RINEX files ending with “PPKRAW” for the rover, “HCN” for the GNSS base station, and “\*.20o” for the TUSAGA-Aktif reference stations (IZMI, CESM, KIKA), were first imported, and following the process, the corrected camera locations were saved as a CSV file.



Figure 2. UAV System: DJI Phantom 4 RTK (Top), CHCN X91 GNSS receiver (Bottom) used in the study

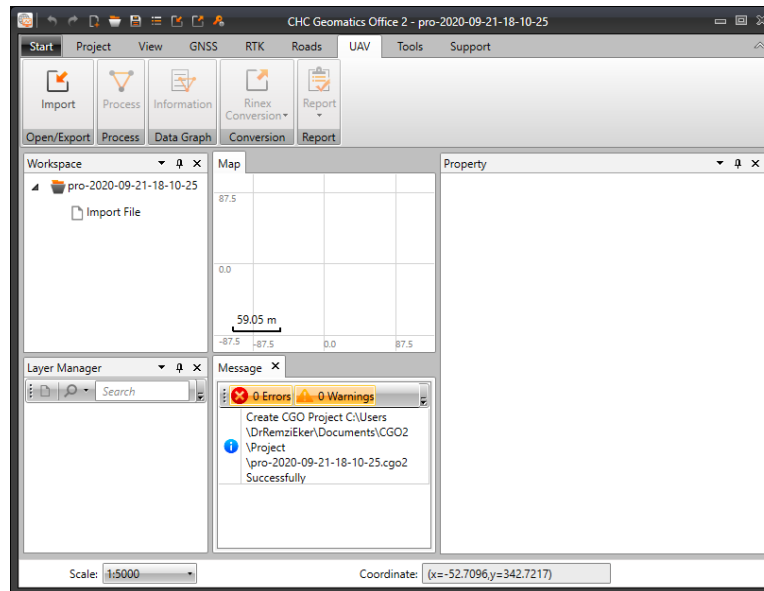


Figure 3. Interface of CHC Geomatics Office 2 software

### 2.3. Photogrammetric data processing

The UAV-based images were processed in the Agisoft Metashape Professional using a standard workflow. The images acquired in RTK-CORS mode provided camera location information (latitude, longitude, altitude, and accuracy) tagged by the UAV system to EXIF data. The camera positions of the images taken in PPK mode were corrected using the data from the GNSS, IZMI, CESM, and KIKA fixed stations and recorded as a CSV file for each station. Later, the images and corrected location information were imported from these files to the Metashape software and image orientation was performed. The images were aligned in the “Reference pre-selection” mode. The option of accuracy was selected as “medium” and the limit key points and tie points were set as 40,000 and 4000, respectively. After the images were aligned, camera positions were optimized in four scenarios for each method: (1) using only cameras without GCPs, (2) using cameras with one GCP, (3) using cameras with two GCPs, and (4) using cameras with three GCPs. The remaining GCPs were then used as checkpoints for the accuracy calculation and a high-quality reconstruction of the dense point cloud was conducted. The orthomosaics and DEMs were created in photogrammetric workflow of Metashape software, and exported with spatial resolution of 5 cm and 10 cm, respectively.

### 2.4. Evaluating accuracy of the UAV RTK/PPK methods

In the comparison of the UAV RTK/PPK methods (Table 1), first, the accuracy of the corrected camera positions in X (easting), Y (northing), and Z (altitude) was used. In addition, the average error rates of the camera locations computed in the photo alignment and optimization process for X, Y, Z, XY, and in total were compared. In here, X error (m) is root mean square (RMS) error for X coordinate for all the cameras, Y error

(m) is RMS error for Y coordinate for all the cameras, XY error (m) is RMS error for X and Y coordinates for all the cameras, Z error (m) is RMS for Z coordinate for all the cameras, and Total error (m) is RMS error for X, Y, Z coordinates for all the cameras, which is calculated by following equation (Agisoft Metashape User Manual, 2019):

$$Total\ error = \sqrt{\frac{\sum_{i=1}^n [(X_{i,est} - X_{i,in})^2 + (Y_{i,est} - Y_{i,in})^2 + (Z_{i,est} - Z_{i,in})^2]}{n}} \quad (1)$$

where  $X_{i,in}$  is input value for X coordinate for i camera position,  $X_{i,est}$  is estimated value for X coordinate for i camera position,  $Y_{i,in}$  is input value for Y coordinate for i camera position,  $Y_{i,est}$  is estimated value for Y coordinate for i camera position,  $Z_{i,in}$  is input value for Z coordinate for i camera position, and  $Z_{i,est}$  is estimated value for Z coordinate for i camera position.

Table 1. UAV RTK/PPK methods in the comparison

No	Methods	Definition
1	M1	RTK-CORS method
2	M2	PPK method using GNSS base station data (PPK-GNSS)
3	M3	PPK method using IZMI reference station data (PPK-IZMI)
4	M4	PPK method using CESM reference station data (PPK-CESM)
5	M5	PPK method using KIKA reference station data (PPK-KIKA)

Georeferencing error rates of the models (X, Y, Z, and total) were also compared using nine GCPs surveyed. These error rates are RMS error for X, Y, Z coordinates for a GCP location/check point (Agisoft Metashape User Manual, 2019). For this process, four scenarios were carried out for both the RTK and PPK methods: (1) using only cameras without any GCPs, (2) using cameras with one GCP, (3) using cameras with two GCPs, and (4) using cameras with three GCPs. The aim

was to evaluate the accuracy of the RTK/PPK methods without using GCPs, and to determine the necessity of using some GCPs to improve accuracy.

In addition, differences in the Z direction of the DEMs were evaluated by calculating RMS error rates for different surface objects over six different surface types (roads, shadows, shrubs, boulders, trees, and ground). For this aim, ArcGIS 10.6 software was used to manually create 480 artificial GCPs with a regular distribution for each surface type. In RMS error calculation, the DEMs generated from all PPK methods were compared to the DEM generated using the RTK method. In addition, the DEMs generated via the PPK methods were also compared to the DEM generated via the PPK method based on the GNSS base station.

### 3. Results and Discussion

In this study, two UAV flights (one in RTK and one in PPK) were carried out using the same flight plan at the same altitude (120 m a.g.l.), with 186 images acquired in RTK mode and 192 images acquired in PPK mode. All camera positions were fixed when the base RINEX files from the GNSS receiver and the IZMI station were used. However, 182 cameras were fixed when the base RINEX file from the CESM station was used, whereas 190 cameras were fixed when the base RINEX file from the KIKA station was used. In the photogrammetric analysis of all RTK and PPK methods, only two images could not be aligned. In order to achieve centimeter-level accuracy with the UAV system, a high-quality, multi-frequency GNSS receiver mounted to a platform is needed. The GNSS receiver must at the least handle both L1 and L2 frequencies. The level of absolute accuracy depends on the correction data from the static base-station logging. If the base station is close to the rover (i.e., UAV platform), the amount of time necessary to ensure quality positioning is generally reduced, thus enabling better correction data to be logged by the GNSS receiver on the platform (Rydland and Densmore, 2012). According to White Paper on drone survey accuracy (White Paper, 2018), every 10 km in distance adds 1 cm to the RMS error rate, and vertical accuracy suffers more than horizontal accuracy. In addition to the distance between base station and rover, elevation difference has an important effect on accuracy. Accuracy will be worse with elevation differences of more than 500 m (White Paper, 2018). In the RTK/PPK methods, when the base station is set up on an unknown point, the GNSS receiver should log the GPS data for a more than 3 h. If the base station is established on a known point, the absolute accuracy will depend on how accurately the location of the base station was measured. In the present study, both RTK and PPK methods were based on corrections from base stations where locations were accurately known. Another important requirement in achieving centimeter-level absolute accuracy is the time interval of the continuous logging. For the highest accuracy, a 1-second time interval is best. However, logging at less frequent

intervals of more than 15 s is not recommended (White Paper, 2018). In the present study, a static survey using a base GNSS receiver was conducted at 2-s time intervals, whereas the RINEX files obtained from the TUSAGA-Aktif reference stations recorded continuous logging at 1-s time intervals. In the present study, the three TUSAGA-Aktif reference stations selected as the closest were located 17.7 km (IZMI), 70.7 km (CESM), and 78.1 km (KIKA) from the study area. The elevation differences were 548 m (IZMI), 546 m (CESM), and 362 m (KIKA).

Based on previous explanations regarding the effects of parameters on accuracy, as expected, the PPK-GNSS (M2) provided the best accuracy in camera locations, whereas the PPK-CESM (M4) provided the worst (Table 2, Figure 4). The greatest deviations in accuracy values for all directions (X, Y, and Z) resulted from M4, where both the distance to the rover and the elevation difference were beyond the range of recommended values. The M1 method resulted in worse accuracy in the Z direction compared to the accuracy in the X and Y directions, whereas all other methods resulted in better accuracy in the Z direction, especially in comparison with accuracy in the Y direction.

The lowest error average of the computed camera locations resulted from all scenarios of the M2, as expected (Table 3). Although the M1 resulted in lower errors in both X and Y in comparison to the M3, errors in Z were higher than with the M3. However, the total error of the M3 method was also lower than that of the M1. All scenarios of the M4 resulted in the highest error rates in computing camera locations. All scenarios of the M5 method resulted in lower error rates than the M4. In addition, the use of GCPs together with cameras in the photo alignment and optimization processes did not have a significant impact on the average error of the computed camera locations in the photogrammetric analysis.

When the models were compared in terms of georeferencing errors based on checkpoints (GCPs not used together with cameras in the process of optimizing camera positions), the lowest total RMS error rates were obtained with all scenarios of M2 (Table 4). The results showed that the short-baseline PPK method yielded the best results compared to all the other methods used in the present study. Even though errors in the Z direction for the M2 were lower than those in the Y direction, georeferencing errors in the Z direction were higher than the errors in both X and Y directions. For all methods except the M2, using GCP together with cameras enabled reduction of errors, especially in the Z direction. Using GCPs together with cameras did not provide significant reduction of errors in either the X or Y directions. Moreover, using GCPs together with cameras did not lower total georeferencing errors under 10 cm for the long-baseline methods (M4 and M5). When more than two GCPs were used together with the cameras, similar rates were obtained with the M1, M2, and M3 for errors in the Z direction.

Table 2. Camera position accuracy with RTK and PPK methods

Methods	Statistics	X (m)	Y(m)	Z(m)
M1	Min	0.0116	0.0089	0.0167
	Max	0.0315	0.0176	0.0438
	Mean	0.0145	0.0138	0.0261
	SD	0.0015	0.0010	0.0026
M2	Min	0.0057	0.0074	0.0057
	Max	0.0095	0.0109	0.0087
	Mean	0.0065	0.0084	0.0066
	SD	0.0005	0.0005	0.0005
M3	Min	0.0149	0.0198	0.0138
	Max	0.0213	0.0257	0.0178
	Mean	0.0164	0.0209	0.0147
	SD	0.0008	0.0008	0.0006
M4	Min	0.0222	0.0295	0.0227
	Max	0.0723	0.0681	0.0387
	Mean	0.0366	0.0414	0.0288
	SD	0.0146	0.0090	0.0037
M5	Min	0.0229	0.0302	0.0234
	Max	0.0350	0.0496	0.0381
	Mean	0.0267	0.0359	0.0273
	SD	0.0025	0.0034	0.0024

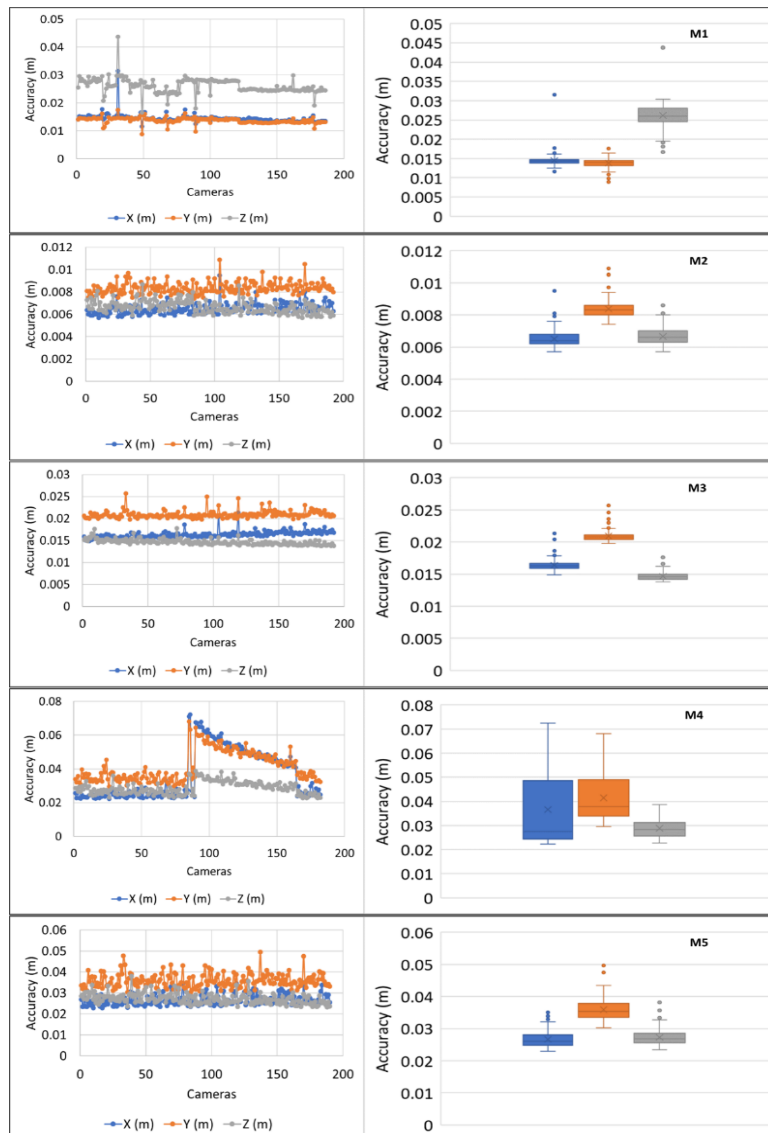


Figure 4. Camera position accuracy obtained with RTK and PPK methods

Table 3. Average error rates of computed camera locations in photogrammetric analysis of UAV data

Methods	Baseline	Baseline	X	Y	Z	XY	Total
M1			0.23	0.27	0.86	0.35	0.93
M1 + 1 GCP	Unknown	Unknown	0.23	0.27	0.89	0.36	0.95
M1 + 2 GCP			0.23	0.27	0.88	0.36	0.95
M1 + 3 GCP			0.23	0.27	0.88	0.36	0.95
M2					0.06	0.11	0.15
M2 + 1 GCP	0.2	<25	0.06	0.11	0.15	0.12	0.19
M2 + 2 GCP			0.06	0.11	0.15	0.12	0.19
M2 + 3 GCP			0.06	0.11	0.15	0.12	0.19
M3					0.32	0.52	0.45
M3 + 1 GCP	17.7	548	0.32	0.52	0.45	0.61	0.76
M3 + 2 GCP			0.32	0.52	0.48	0.61	0.78
M3 + 3 GCP			0.32	0.52	0.48	0.61	0.78
M4					2.92	2.63	4.62
M4 + 1 GCP	70.7	546	3.01	2.90	4.73	4.18	6.31
M4 + 2 GCP			2.95	3.02	4.80	4.22	6.40
M4 + 3 GCP			3.07	2.98	4.83	4.28	6.45
M5					0.89	1.14	1.41
M5 + 1 GCP	78.1	362	0.86	1.18	1.42	1.46	2.03
M5 + 2 GCP			0.86	1.21	1.42	1.48	2.05
M5 + 3 GCP			0.87	1.23	1.42	1.51	2.07

Table 4. Georeferencing error rates of models based on checkpoints

Methods	Baseline	Baseline	Number of	X	Y	Z	XY	Total
M1			9	2.38	2.34	9.43	3.34	10.01
M1 + 1 GCP	Unknown	Unknown	8	1.92	2.02	6.09	2.79	6.69
M1 + 2 GCP			7	2.05	2.31	6.22	3.09	6.95
M1 + 3 GCP			6	1.99	1.89	6.21	2.75	6.79
M2					9	1.72	2.91	4.81
M2 + 1 GCP	<0.25	<25	8	1.84	1.49	4.63	3.57	5.85
M2 + 2 GCP			7	2.21	2.71	4.66	3.50	5.82
M2 + 3 GCP			6	2.38	2.49	5.30	3.44	6.32
M3					9	5.82	5.65	10.31
M3 + 1 GCP	17.7	548	8	5.03	5.62	7.34	7.54	10.53
M3 + 2 GCP			7	5.11	6.06	5.67	7.93	9.75
M3 + 3 GCP			6	5.47	6.27	6.52	8.32	10.57
M4					9	10.54	20.65	53.84
M4 + 1 GCP	70.7	546	8	13.75	18.20	22.01	22.81	31.70
M4 + 2 GCP			7	13.44	18.23	29.38	22.65	37.10
M4 + 3 GCP			6	12.99	19.36	27.18	23.32	35.81
M5					9	6.46	16.25	12.93
M5 + 1 GCP	78.1	362	8	5.97	15.60	10.60	16.70	19.78
M5 + 2 GCP			7	6.19	16.24	11.76	17.37	20.98
M5 + 3 GCP			6	6.67	17.06	7.83	18.31	19.91

Model accuracy obtained by photogrammetry depends on many factors, such as image quality, camera calibration, flight plan characteristics, the SfM algorithm, and surface texture and albedo (Zhang et al., 2019). In the present study, two flights were carried out using the same platform from the same altitude with the same flight plan. For both flights, image quality values calculated during the photogrammetric process varied between 0.65 and 0.85. All image datasets from each method were processed using the same SfM algorithm. The remaining factor affecting model accuracy was assumed to be surface texture. Thus, in this study, the models were also compared by calculating RMS error rates in the Z direction for different surface objects such as roads, boulders, ground, shrubs, trees, and shadows. The surface type “road” is a man-made infrastructure with a certain geometry that may have a tarmacked or

graveled surface. The surface type “boulder” refers to rocks of varying diameter and stones that are too large for a person to move. The type “ground” means a surface covered by bare earth, short grasses, or pebbles. Although boulders, roads, and ground are solid types of surface, shrubs and trees are not solid. They form hollow structures that have an important effect on photogrammetric modeling. First, the M1 method was considered as the reference data for comparing the PPK methods, and the M2 method was considered as the reference for comparing the short-baseline PPK method with the long-baseline PPK methods (Figure 5).



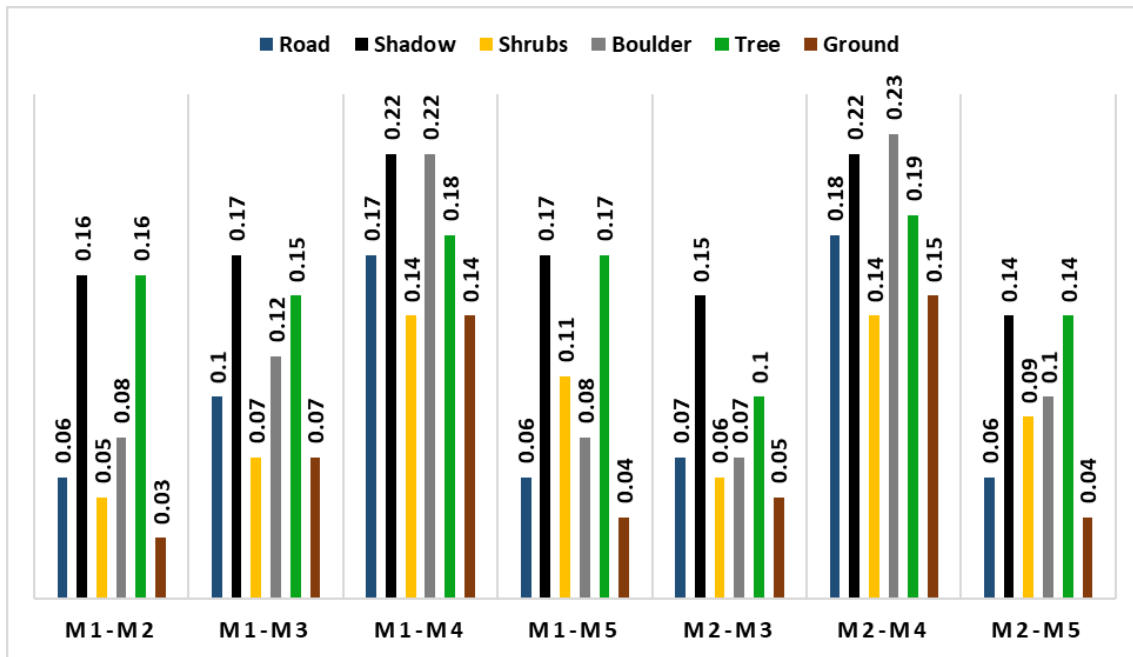


Figure 5. RMS errors (m) calculated from DEMs generated from methods using only cameras

The M1 and M2 methods were chosen as reference because the lower error rates are expected from them relative to other long-baseline PPK methods. The RMS error rates were then calculated from the DEMs generated from the methods using only cameras. In other words, the GCPs were not used together with cameras in the process of optimizing the cameras, because the aim of use RTK/PPK methods in UAV photogrammetry is to eliminate the need of GCP. Lower RMS error rates were obtained for the surface types of “ground”, “roads”, and “shrubs” than for other types. For the surface type “trees”, the RMS error between the RTK and PPK methods was more than 15 cm. The lowest RMS error was 10 cm between M2 and M3 for the surface type “trees”. The RMS errors for “shadows” were similar to those for “trees”, since they are mostly located in gaps between trees. Because of the irregular, complex, and

hollow-shaped tree crowns, the RMS error values were higher than for other surface types. An elevation profile of the surface type “boulders” was drawn for each of the RTK/PPK methods (Figure 6). According to this profile, in the DEM generated by the M1 method, the elevations modeled were mostly higher than with the other methods. Even though a similar pattern in the elevation profiles of the surface objects was observed, important fluctuations in the Z values were seen in the profiles of objects. These caused an increase in RMS error among the models. This was caused by shifts in the X and Y directions that prevented the elevation profile of the same line to be drawn between two points located in exactly the same position over the reference DEM (Figure 7). Elevation profiles are also given for other surface types: roads in Figure 8, ground in Figure 9, and trees in Figures 10 and 11.

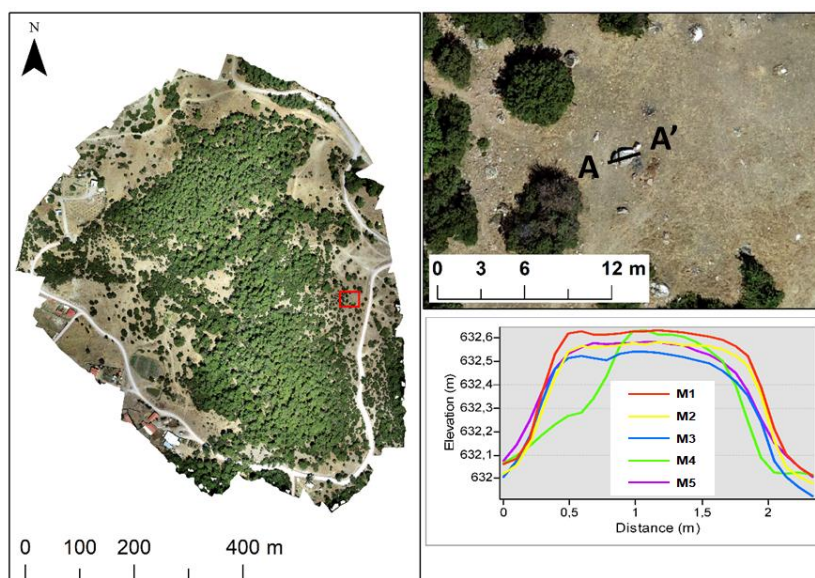


Figure 6. Elevation profile of a boulder

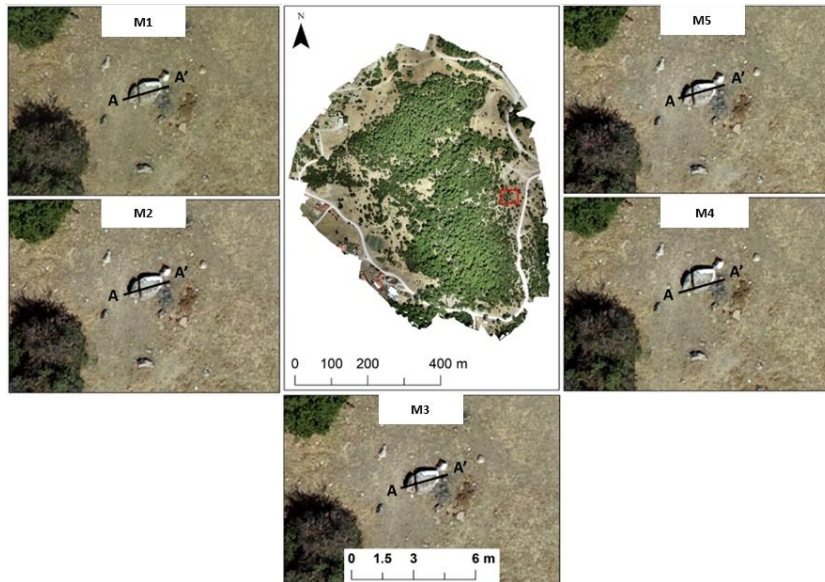


Figure 7. Position of line between two points (A and A') drawn over the reference orthomosaic (M1) and its locational difference on other models (M2, M3, M4, and M5)

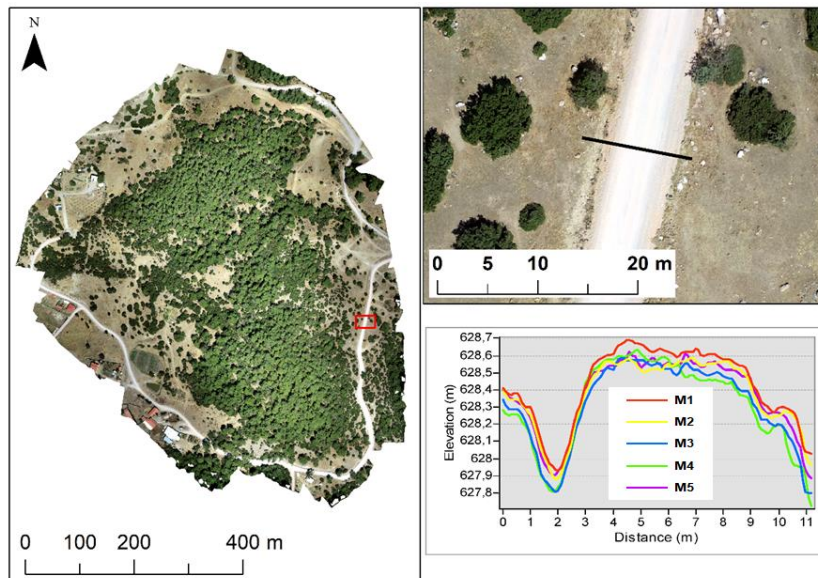


Figure 8. Elevation profile of a road

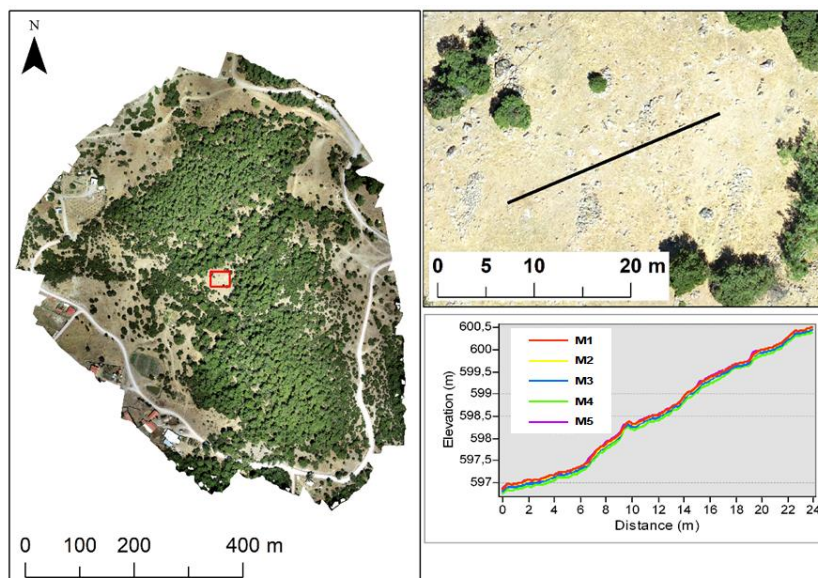


Figure 9. Elevation profile of the ground

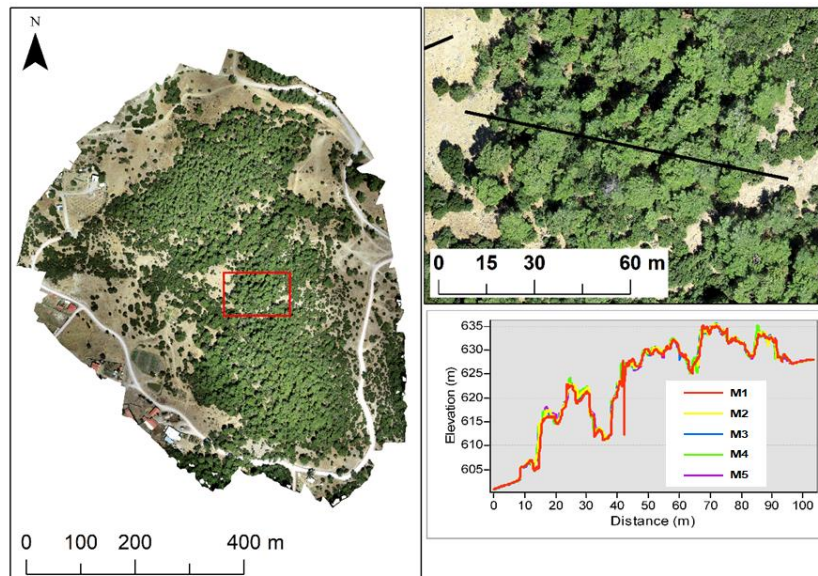


Figure 10. Elevation profile of trees

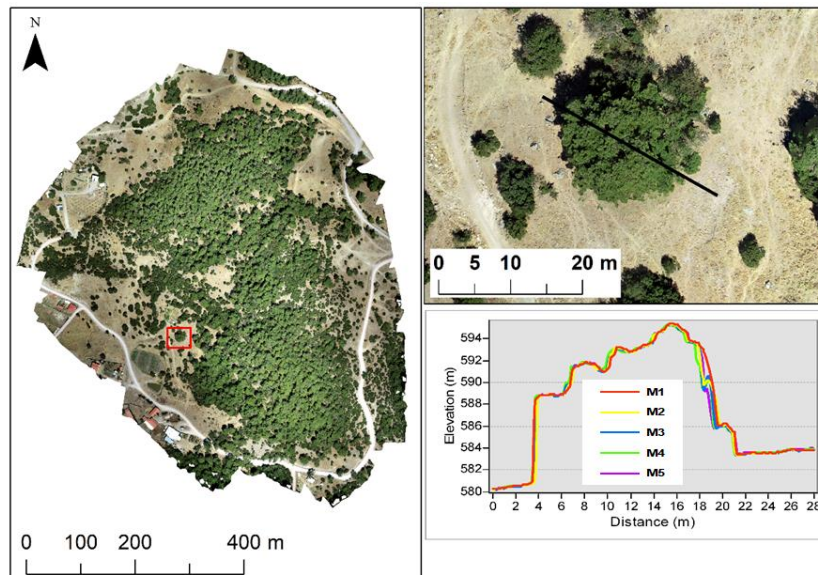


Figure 11. Elevation profile of a single tree

#### 4. Conclusion

The utilization of direct georeferencing approaches (e.g., RTK and PPK) using a GNSS receiver integrated into a UAV provides the potential for avoiding/mitigating the need for GCPs. In the present study, we tested UAV-PPK and UAV-RTK methods by comparing them in the mapping of different surface types. In this study, five methods were compared: (1) RTK-CORS, (2) PPK using GNSS base station data (PPK-GNSS), (3) PPK using IZMI reference station data (PPK-IZMI), (4) PPK using CESM reference station data (PPK-CESM), and (5) PPK using KIKA reference station data (PPK-KIKA). The study concluded that the lowest error rate in the corrected camera locations via the differential GNSS solution was obtained by the PPK-GNSS method, as expected. However, it was determined that both RTK-CORS and PPK-IZMI provided similar accuracy rates since both methods used the same reference station to acquire corrections. All methods were found to provide camera

position accuracy calculated as less than 5 cm. In addition to positional corrections of the cameras by differential GNSS solutions, the error rates of camera locations computed via the alignment process in the photogrammetric analysis were within similar ranges. This study concluded that using GCPs together with corrected camera positions in the image alignment process did not significantly affect the error of the computed camera locations in the photogrammetric analysis. However, using GCPs could still have a significant impact on the georeferencing error of the models obtained via the photogrammetric process. This impact becomes especially important when long-baseline methods such as RTK-CORS and PPK methods use corrections obtained from TUSAGA-Aktif reference stations. In addition, the short-baseline PPK method using GNSS-based corrections was not significantly affected by using GCPs. It can be concluded that when long-baseline differential GNSS solutions are preferred, using GCPs remains a

necessity for the image alignment process in addition to their usage as checkpoints.

In this study, the models generated using only image locations were also compared by calculating the RMS error rates in the Z direction for different surface objects such as roads, boulders, ground, shrubs, trees, and shadows. The model obtained via the RTK-CORS method was assumed as the reference in the first comparison, whereas the model obtained via the PPK-GNSS method was assumed as the reference in the second comparison. These comparisons concluded that the lowest RMS error rates were determined over solid-textured surfaces such as ground and roads. The greatest differences in RMS error rates were obtained over trees and shadowed areas. The study determined that in models generated by applying different methods, the error differences could vary greatly, within the range of 3–23 cm, depending on the surface type modeled. Consequently, in such model comparisons, considering the mean RMS error regardless of surface type could be misleading.

**Ethics Committee Approval:** N/A.

**Peer-review:** Externally peer-reviewed.

**Author Contributions:** Concept: R.E.; Design: R.E.; Supervision: A.A.; Resources: R.E.; Data Collection: R.E. and E.A.; Analysis: R.E. and E.A.; Literature Search: R.E.; Writing Manuscript: R.E.; Critical Review: A.A.

**Conflict of Interest:** The authors have no conflicts of interest to declare.

**Financial Disclosure:** The authors declared that this study has received no financial support

**Cite this paper as:** Eker, R., Alkan, E., Aydın, A., 2021. A Comparative Analysis of UAV-RTK and UAV-PPK Methods in Mapping Different Surface Types, *European Journal of Forest Engineering*, 7(1):12-25.

## References

- Abdelkader, M., Shaqura, M., Claudel, C.G., Gueaieb, W., 2013. A UAV based system for real time flash flood monitoring in desert environments using Lagrangian microsensors. International Conference on Unmanned Aircraft Systems (ICUAS), Atlanta, GA, USA, 25-34.
- Adams, M.S., Bühler, Y., Fromm, R., 2018. Multitemporal accuracy and precision assessment of unmanned aerial system photogrammetry for slope-scale snow depth maps in alpine terrain. *Pure and Applied Geophysics*, 175: 3303–3324.
- Agisoft Metashape User Manual, 2019. Agisoft Metashape User Manual: Professional Edition, Version 1.5 [https://www.agisoft.com/pdf/metashape-pro\\_1\\_5\\_en.pdf](https://www.agisoft.com/pdf/metashape-pro_1_5_en.pdf).
- Agüera-Vega, F., Carvajal-Ramírez, F., Martínez-Carricondo, P., 2017. Assessment of photogrammetric mapping accuracy based on variation ground control points number using unmanned aerial vehicle. *Meas J Int Meas Confed*, 98: 221–227.
- Akgul, M., Yurtseven, H., Gulci, S., Akay, A.E., 2018. Evaluation of UAV- and GNSS-based DEMs for earthwork volume. *Arabian Journal for Science and Engineering*, 43(4): 1893–1909.
- Annis, A., Nardi, F., Petroselli, A., Apollonio, C., Arcangeletti, E., Tauro, F., Belli, C., Bianconi, R., Grimaldi, S., 2020. UAV-DEMs for Small-Scale Flood Hazard Mapping. *Water*, 12, 1717.
- Bühler, Y., Adams, M.S., Bösch, R., Stoffel, A., 2016. Mapping snow depth in alpine terrain with unmanned aerial systems (UASs): Potential and limitations. *Cryosphere*, 10: 1075–1088.
- Campana, S., 2017. Drones in archaeology. State-of-the-art and future perspectives. *Archaeol Prospect*, 24: 275-296.
- Carvajal, F., Agüera, F., Pérez, M., 2011. Surveying a landslide in a road embankment using unmanned aerial vehicle photogrammetry. The International Archives of the Photogrammetry, Remote Sensing and Spatial Information Sciences XXXVIII (Part 1/C22): 201–206.
- Colomina, I., Molina, P., 2014. Unmanned aerial systems for photogrammetry and remote sensing: a review. *ISPRS Journal of Photogrammetry and Remote Sensing*, 92: 79-97.
- De Michele, C., Avanzi, F., Passoni, D., Barzaghi, R., Pinto, L., Dosso, P., Ghezzi, A., Gianatti, R., Della Vedova, G., 2016. Using a fixed-wing UAS to map snow depth distribution: An evaluation at peak accumulation. *Cryosphere*, 10: 511–522.
- Eisenbeiss, H., 2009. UAV photogrammetry. Ph.D. Thesis, Institute of Geodesy and Photogrammetry, ETH Zurich, Zurich, Switzerland, 235.
- Eker, R., Aydın, A., 2021. Long-term retrospective investigation of a large, deep-seated, and slow-moving landslide using InSAR time series, historical aerial photographs, and UAV data: The case of Devrek landslide (NW Turkey). *Catena*, 196: 104895.
- Eker, R., Aydın, A., Hübl, J., 2018. Unmanned aerial vehicle (UAV)-based monitoring of a landslide: Gallenzerkogel landslide (Ybbs-Lower Austria) case study. *Environ. Monitor. Assess.* 190: 14.
- Eker, R., Bühler, Y., Schlägl, S., Stoffel, A., Aydın, A., 2019. Monitoring snow cover ablation with very high spatial resolution remote sensing techniques. *Remote Sensing*, 11(6): 699.
- Evaerts, J., 2008. The use of unmanned aerial vehicles (UAVs) for remote sensing and mapping. Proceeding of the The International Archives of the Photogrammetry, Remote Sensing and Spatial Information Sciences XXXVII (Part B1. Beijing): 1187–1191.
- Fernández-Hernandez, J., González-Aguilera, D., Rodríguez-Gonzálvez, P., Mancera-Taboada, J., 2015. Image-based modelling from Unmanned Aerial Vehicle (UAV) photogrammetry: An effective, low-cost tool for archaeological applications. *Archaeometry*, 57: 128-145.
- Giordan, D., Manconi, A., Remondino, F., Nex, F., 2017. Use of unmanned aerial vehicles in monitoring application and management of natural hazards. *Geomatics, Natural Hazards and Risk*, 8: 1–4.
- Gomez, C., Purdie, H., 2016. UAV- based Photogrammetry and Geocomputing for Hazards and Disaster Risk Monitoring – A Review. *Geoenvironmental Disasters*, 3: 23.
- Gülci, S., 2019. The determination of some stand parameters using SfM-based spatial 3D point cloud in forestry studies:

- An analysis of data production in pure coniferous young forest stands. *Environ Monit Assess*, 191: 495.
- Harwin, S., Lucieer, A., Osborn, J., 2015. The Impact of the Calibration Method on the Accuracy of Point Clouds Derived Using Unmanned Aerial Vehicle Multi-View Stereopsis. *Remote Sensing*, 7: 11933–11953.
- Hofmann-Wellenhof, B., Lichtenegger, H., Wasle, E., 2007. GNSS–Global Navigation Satellite Systems: GPS, GLONASS, Galileo and More. Springer Science & Business Media, New York, NY, USA, ISBN 3211730176.
- Honkavaara, E., Saari, H., Kaivosoja, J., Pölönen, I., Hakala, T., Litkey, P., Mäkyänen, J., Pesonen, L., 2013. Processing and Assessment of Spectrometric, Stereoscopic Imagery Collected Using a Lightweight UAV Spectral Camera for Precision Agriculture. *Remote Sens*, 5: 5006-5039.
- James, M.R., Robson, S., 2014. Mitigating systematic error in topographic models derived from UAV and ground-based image networks. *Earth Surf Process Landf*, 39: 1413–1420.
- James, M.R., Robson, S., d’Oleire-Oltmanns, S., Niethammer, U., 2017. Optimising UAV topographic surveys processed with structure-from-motion: Ground control quality, quantity and bundle adjustment. *Geomorphology*, 280: 51–66.
- Jurjevic, L., Gašparovic, M., Milas, A.S., Balenovi, I., 2020. Impact of UAS Image Orientation on Accuracy of Forest Inventory Attributes. *Remote Sensing*, 12: 404.
- Langhammer, J., Lendziach, T., Miřijovský, J., Hartvich, F., 2017. UAV-Based Optical Granulometry as Tool for Detecting Changes in Structure of Flood Depositions. *Remote Sensing*, 9(3): 240.
- Lindner, G., Schraml, K., Mansberger, R., Hübl, J., 2016. UAV monitoring and documentation of a large landslide. *Appl Geomat*, 8(1): 1–11.
- Lisein, J., Pierrot-Deseilligny, M., Bonnet, S., Lejeune, P., 2013. A Photogrammetric Workflow for the Creation of a Forest Canopy Height Model from Small Unmanned Aerial System Imagery. *Forests*, 4(4): 922–944.
- Lucieer, A., de Jong, S.M., Turner, D., 2014. Mapping landslide displacements using structure from motion (SfM) and image correlation of multi-temporal UAV photography. *Prog Phys Geogr*, 38: 97–116.
- Mateos, R.M., Azañón, J.M., Roldán, F.J., Notti, D., Pérez-Peña, V., Galve, J.P., Pérez-García, J.L., Colomo, C.M., Gómez-López, J.M., Montserrat, O., Devantery, N., Lamas-Fernández, F., Fernández-Chacón, F., 2017. The combined use of PSInSAR and UAV photogrammetry techniques for the analysis of the kinematics of a coastal landslide affecting an urban area (SE Spain). *Landslides*, 14(2): 743–754.
- Matese, A., Toscano, P., Di Gennaro, S.F., Genesio, L., Vaccari, F.P., Primicerio, J., Gioli, B., 2015. Intercomparison of UAV, aircraft and satellite remote sensing platforms for precision viticulture. *Remote Sensing*, 7 (3): 2971-2990.
- Mekik, Ç., Yıldırım, Ö., Bakıcı, S., 2011. The Turkish real time kinematic GPS network (TUSAGA-Aktif) infrastructure. *Scientific Research and Essays*, 6(19): 3986-3999.
- Nebiker, S., Annen, A., Scherrer, M., Oesch, D., 2008. A lightweight multispectral sensor for micro-UAV—opportunities for very high resolution airborne remote sensing. Proceeding of the International Archives of the Photogrammetry, Remote Sensing and Spatial Information Sciences XXXVII (Part B1. Beijing), 1193–1199.
- Niethammer, U., Rothmund, S., Joswig, M., 2009. UAV-based remote sensing of the slow-moving landslide super-Sauze. In: Malet JP, Remaitre A, Boogard T (eds) Proceedings of the International Conference on Landslide Processes: From geomorphologic mapping to dynamic modeling. CERG Editions, Strasbourg, France, 69–74.
- Radoglou-Grammatikis, P., Sarigiannidis, P., Lagkas, T., Moscholios, I., 2020. A compilation of UAV applications for precision agriculture. *Computer Networks*, 172: 107148.
- Rehak, M., Mabillard, R., Skaloud, J., 2013. A micro-UAV with the capability of direct georeferencing. ISPRS – Int Arch Photogramm Remote Sen Spatial Inform Sci XL-1/W2: 317-323.
- Remondino, F., Barazzetti, L., Nex, F., Scaioni, M., Sarazzi, D., 2011. UAV photogrammetry for mapping and 3D modeling - Current status and future perspectives. In: Int Archives of Photogrammetry, Remote Sensing and Spatial Information Sciences, 38(1/C22). ISPRS Conference UAV-g, Zurich, Switzerland.
- Rydland, P.H. Jr., Densmore, B.K., 2012. Methods of practice and guidelines for using survey-grade global navigation satellite systems (GNSS) to establish vertical datum in the United States Geological Survey: U.S. Geological Survey Techniques and Methods, Book 11, Chapt. D1, 102.
- Sanz-Ablanedo, E., Chandler, J., Rodríguez-Pérez, J., Ordóñez, C., Sanz-Ablanedo, E., Chandler, J.H., Rodríguez-Pérez, J.R., Ordóñez, C., 2018. Accuracy of unmanned aerial vehicle (UAV) and SfM photogrammetry survey as a function of the number and location of ground control points used. *Remote Sensing*, 10: 1606.
- Saroglou, C., Asteriou, P., Zekkos, D., Tsiambaos, G., Clark, M., Manousakis, J., 2018. UAV-based mapping, back analysis and trajectory modeling of a coseismic rockfall in Lefkada island, Greece. *Nat Hazards Earth Syst Sci*, 18: 321-333.
- Shervais, K., 2015. Structure from Motion, Introductory Guide. Retrieved 27 July 2016 from <https://www.unavco.org/education/resources/educational-resources/lesson/field-geodesy/module-materials/sfm-intro-guide.pdf>.
- Sugiura, R., Noguchi, N., Ishii, K., 2007. Correction of low-altitude thermal images applied to estimating soil water status. *Biosystems Engineering*, 96(3): 301–313.
- Taddia Y, Stecchi F, Pellegrinelli A (2020) Coastal mapping using DJI phantom 4 RTK in post-processing kinematic mode. *Drones* 4: 9.
- Thiel, C., Schmullius, C., 2017. Comparison of UAV photograph-based and airborne lidar-based point clouds over forest from a forestry application perspective. *International Journal of Remote Sensing*, 38(8-10): 2411-2426.
- Tokekar, P., Hook, J.V., Mulla, D., Isler, V., 2016. Sensor planning for a symbiotic UAV and UGV system for precision agriculture. *IEEE Transactions on Robotics*, 32(6): 1498 – 1511.
- Tomaščík, J., Mokroš, M., Surový, P., Grznárová, A., Merganic, J., 2019. UAV RTK/PPK method-An optimal solution for mapping inaccessible forested areas? *Remote Sensing*, 11: 721.
- Torresan, C., Berton, A., Carotenuto, F., Di Gennaro, S.F., Gioli, B., Matese, A., Miglietta, F., Vagnoli, C., Zaldei, A., Wallace, L., 2017. Forestry applications of UAVs in Europe: A review. *International Journal of Remote Sensing*, 38(8-10): 2427-2447.

- Turner, D., Lucieer, A., de Jong, S.M., 2015. Time series analysis of landslide dynamics using an unmanned aerial vehicle (UAV). *Remote Sensing*, 7(2): 1736–1757.
- Vander Jagt, B., Lucieer, A., Wallace, L., Turner, D., Durand, M., 2015. Snow Depth Retrieval with UAS Using Photogrammetric Techniques. *Geosciences*, 5: 264.
- Wallace, L., Lucieer, A., Malenovsky, Z., Turner, D., Vopenka, P., 2016. Assessment of Forest Structure Using Two UAV Techniques: A Comparison of Airborne Laser Scanning and Structure from Motion (SfM) Point Clouds. *Forests*, 7: 62.
- Wallace, L., Lucieer, A., Watson, C., Turner, D., 2012. Development of a UAV-LiDAR system with application to forest inventory. *Remote Sensing*, 4(12): 1519–1543.
- Watts, A.C., Ambrosia, V.G., Hinkley, E.A., 2012. Unmanned aircraft systems in remote sensing and scientific research: Classification and considerations of use. *Remote Sensing*, 4(12): 1671–1692.
- Westoby, M.J., Brasington, J., Glasser, N.F., Hambrey, M.J., Reynolds, J.M., 2012. Structure-from-Motion photogrammetry: A low-cost, effective tool for geoscience applications. *Geomorphology*, 179: 300–314.
- White Paper, 2018. Reaching 1 cm (0.4 in) drone survey accuracy. Available at <https://wingtra.com/mapping-drone-wingtraone/drone-survey-accuracy/wingtra-white-paper-reaching-1cm-drone-survey-accuracy/>.
- Yıldırım, Ö., Mekik, Ç., Bakıcı, S., 2011. TUSAGA-Active(CORS-TR)System, Contributions to The General Directorate of Land Registry and Cadastre. *Geodesy, Geoinformation and Land Management Journal*, Special Issue, 2011(2): 134-139.
- Yuan, C., Zhang, Y., Liu, Z., 2015. A Survey on Technologies for Automatic Forest Fire Monitoring, Detection, and Fighting Using Unmanned Aerial Vehicles and Remote Sensing Techniques. *Canadian Journal of Forest Research*, 45(7): 783–792.
- Zhang, H., Aldana-Jague, E., Clapuyt, F., Wilken, F., Vanacker, V., Van Oost, K., 2019. Evaluating the potential of post-processing kinematic (PPK) georeferencing for UAV-based structure-from-motion (SfM) photogrammetry and surface change detection. *Earth Surf Dyn*, 7: 807–827.